Catalysis Today 459 (2025) 115440

Contents lists available at ScienceDirect

Catalysis Today

journal homepage: www.elsevier.com/locate/cattod

Continuous photothermal gas-phase CO_2 hydrogenation over highly dispersed Ru-Ni on TiO_2 ☆

Arturo Sanz-Marco [a,b,c], Jose L. Hueso [a,b,c,d,e], Víctor Sebastian [a,b,c], Francisco Balas [a,b,c,*], Jesus Santamaria [a,b,c,*]

[a] Instituto de Nanociencia y Materiales de Aragón (INMA)– University of Zaragoza and Consejo Superior de Investigaciones Científicas(CSIC), Mariano Esquillor, s/n. 50018, Zaragoza, Spain
[b] Networking Research Center in Biomaterials, Bioengineering and Nanomedicine (CIBER-BBN), Monforte de Lemos, 3-5, Madrid 28029, Spain
[c] Department of Chemical Engineering and EnvironmentalTechnologies, University of Zaragoza, María de Luna, 3, Zaragoza 50018, Spain
[d] Escuela Politécnica Superior, Universidad de Zaragoza, Ctra. de Cuarte, Huesca 22071, Spain
[e] Instituto de Investigación Sanitaria de Aragón, Centrode Investigación Biomédica de Aragón (CIBA), San Juan Bosco, 13, Zaragoza 50009, Spain

ARTICLE INFO

Keywords:
TiO_2
Photocatalysis
Solar fuels
CO_2hydrogenation
CH_4

ABSTRACT

Photocatalytic and photothermal carbon dioxide (CO_2) hydrogenation are investigated as key strategies for CO_2 depletion by transformation into valuable products. Ni and Ru are well known Sabatier's reaction catalysts. In the present work we study their activity as Ni, Ru and bimetallic nanoparticles over the surface of titanium dioxide (TiO_2) in the photocatalytic reduction of CO_2, following a process of photo-assisted deposition that yield highly dispersed nanoparticles with sizes under 2 nm. Outstanding production of solar fuels was observed from Ni and Ru 2-nm nanoparticles deposited onto P25 TiO_2. The photocatalytic activity tests under light irradiation from low-energy LEDs at different wavelengths, from UV-A at 365 nm to infrared at 940 nm at 523 K, rendered up to 6 % CO_2 conversion under continuous feed, with CO and CH_4 productivities above 5 mmol/g_{cat}·h.

1. Introduction

Maintaining the energy demands of the world's population while protecting the natural environment is a challenging task. Scientific evidence points to anthropogenic CO_2 as the main cause of global warming especially in activities related to power generation and transportation. However, these are basic needs that cannot be avoided, and it is therefore imperative to achieve a sustainable state in the production and use of energy, something that can only be achieved by implementing strategies that reduce the burden of greenhouse gases (GHG) in the atmosphere. However, a record 1.9 GTm of GHG was emitted in 2021 attributed to the rapid post-pandemic growth of worldwide economies and an unexpected surge in coal demand even as the capacity of renewable sources increased [1]. The previsions of the International Energy Agency pointed to 25 GTm of annual emissions if coal sources run to the end of their lifetime. Despite these discouraging developments, the goal to net zero emissions by 2050 is still in the agenda [2].

The search for sustainable fuels and a rational recycle of the emitted gases is therefore an obligation while more efficient alternative energy sources are explored. Among them, valorization of CO_2 containing streams by the production of value-added chemicals using reducing agents from sustainable sources [3–5] seems an ideal approach. This requires the development of efficient industrial processes for capturing the atmospheric CO_2 and converting it via catalytic reduction into carbon monoxide [6], hydrocarbons (like methanol or methane) [7] or carbon oxygenates [8]. It is in these processes where the use of photo-assisted thermal reaction pathways is gaining interest [9–11]. This route has demonstrated an enhanced CO_2 reduction capacity using catalysts with very diverse configurations and metal co-catalysts [12–14], particularly effective in the case of Ni [15] or Ru [16]. The photo-thermal effects depend on several factors based on the optical and electronic structure of the catalysts [17,18]. For instance, nanosized metal clusters deposited on metal oxide semiconductors undergo

☆ "Given his/her/their role as <Executive Guest Editor>, <Jose L. Hueso> had no involvement in the peer review of this article and has no access to information regarding its peer-review. Full responsibility for the editorial process for this article was delegated to another journal editor.";

* Corresponding authors at: Instituto de Nanociencia y Materiales de Aragón (INMA)– University of Zaragoza and Consejo Superior de Investigaciones Científicas (CSIC), Mariano Esquillor, s/n. 50018, Zaragoza, Spain.
E-mail addresses: fbalas@unizar.es (F. Balas), Jesus.Santamaria@unizar.es (J. Santamaria).

https://doi.org/10.1016/j.cattod.2025.115440
Received 13 February 2025; Received in revised form 10 June 2025; Accepted 24 June 2025
Available online 26 June 2025

broadband optical absorption, followed by non-radiative relaxation of photoexcited surface plasmons in the surface of metal nanocomponents [19–23]. From a mechanistic point of view, photo-thermal hydrogenation involves a cascade of photochemical processes at variable time frames (from 10^{-15} s to 1 s), which controlling step depends on the nature of the catalyst, reactants and reaction conditions: either gas or liquid phase reactions [7,18]. Generally, the main steps in a photo-assisted process are (i) light absorption and subsequent excitation of an electron through the semiconductor band gap, which in turn produces an electron-hole pair, (ii) migration of electrons and holes to reduction and oxidation sites at the surface of the semiconductor and (iii) surface reactions that involve adsorbed reactants and further reduction and oxidation processes [20].

The most common catalyst used in photocatalysis is titanium dioxide (TiO_2), usually with adequate surface modifications [24–26]. For photo-thermal applications, these consist in the deposition of nanosized metal clusters, whereby metal nanoparticles improve the photo-generated charge carrier separation acting as an electron sink [27], along with the formation of catalytically active sites [28]. For this purpose, photo-deposition has emerged as an efficient alternative for synthesizing metal/semiconductor hybrids [29–31]. Compared with other metal decoration procedures that need high temperature, an additional redox agent, electric potential, or multi-step processing, the photo-induced reduction method requires only the irradiation of a light source at the adequate wavelength. With this technique, the size of metal clusters can be controlled by adjusting the concentration of the metal precursor, irradiation time and power [32]. Photo-deposition allows a better dispersion of the metal clusters on the surface of the semiconductor, with smaller particle sizes and higher catalytic activity. In terms of photothermal catalysis, these dispersed nanosized metallic particles confer the capacity to transfer the electron energy into thermal energy, which further heats up the catalyst surface and enhances the redox process [19].

Keeping in mind the objective of net-zero emissions, our approach pursues developing photocatalysts based on the abundant TiO_2 with high activity in virtually the full solar spectrum. In the present work, Ni and Ru metal nanoparticles were photo-deposited onto P25 TiO_2 support to produce photocatalysts for CO_2 hydrogenation in an expanded wavelength range. The precipitation on TiO_2 of metal Ni from Ni^{2+} salts ($E^0 = -0.257$ V) has been described to synthesize photocatalysts for the CO_2 reduction in the UV to visible light range [31], where the total amount of Ni metal deposited on TiO_2 was about of a 0.6 % of the total weight of the material. On the other hand, the remarkable difference between reduction potentials of Ni and Ru cations (Ru^{3+}/Ru^{2+} at $E^0 = 0.2487$ V [33]) burdens the photo-deposition of both metals in a single step. Instead, a two-step process was necessary to first deposit Ni onto TiO_2 under UV irradiation to produce Ni-TiO_2, which after separation and drying serves as a suitable support for the photo-deposition of Ru under UV irradiation. In these conditions, Ni clusters underwent a light-induced galvanic replacement process with the Ru cations [34], in which the overall amount of precipitated metal on the TiO_2 support was similar under both processes. With this process, bimetallic Ru:Ni nanoparticles were deposited over the surface of TiO_2, which were catalytically active towards the CO_2 hydrogenation at low pressure and mild temperature conditions, with a higher CO_2 conversion and long term CH_4 selectivity than their monometallic (Ni or Ru) counterparts.

2. Experimental section

2.1. LED-assisted photo-deposition of metals onto P25 TiO_2 nanoparticles

The synthesis of metal-loaded TiO_2 nanoparticles was performed using the photo-assisted metal deposition procedure already published elsewhere [31]. Briefly, nanosized P25 (Degussa, Germany) was alternatively dispersed in 17 ml of a 2.5-mM $NiCl_2$ aqueous solution (Ni: 45 % mol, Sigma-Aldrich) or 8 ml of a 0.3-mM $RuCl_3$ aqueous solution (Ru: 45-55 % mol, Sigma-Aldrich) at 25ºC under N_2 flow. After degassing for 20 min, 1 ml of methanol (CH_3OH, Sigma-Aldrich) was added to the suspension and further exposed to UV irradiation under two LED lamps (OSRAM LED Engin, Wilmington MA) at 365 nm for 270 s for Ni deposition and for 600 s for Ru deposition, under continuous magnetic stirring. The obtained dark-colored solids were separated after centrifugation at 7500 rpm for 5 min, washed three times with double-deionized water and finally dried at 100 ºC for 12 h. Bimetallic materials were prepared performing the Ru photo-deposition procedure over the Ni loaded TiO_2. These nanomaterials were prepared at the Synthesis of Nanoparticles Unit 9 of the ICTS "NANBIOSIS" at the University of Zaragoza.

2.2. Characterization techniques

Photo-deposited metals on the nanosized TiO_2 substrates were comprehensively analyzed using a variety of techniques. The X-ray diffraction (XRD) patterns were collected in a Bruker D8 Advance Diffractometer (Bruker Corporation, Billerica MA) equipped with a (002)-Ge monochromator using the $CuK_{\alpha 1}$ edge at 1.5405 Å. The solid-state diffuse reflectance UV–vis spectra were recorded in a Shimazdu UV-2600 UV–vis/ NIR spectrophotometer (Shimazdu, Kyoto, Japan) using a 60-mm UV–vis/NIR integrating sphere. Temperature-programmed reduction (TPR) tests were performed in a Quantachrome ChemBET Pulsar TPR/TPD analyzer (Quantachrome Instruments, Boynton Beach, FL) equipped with a Thermal Conductivity Detector (TCD). Before TPR tests, the samples were submitted to a thermal pretreatment at 100 ºC during 1 h under a 20 ml/min N_2 flowing to remove ambient moisture and adsorbed species in the surface of our photocatalysts. For the TPR tests, the gas flowing changed to a 10 % H_2:Ar (20 ml/min) gas mixture and temperature was raised at a 10 ºC/min up to 700 ºC, and held for 15 min before letting cool down to room temperature. The metal loading of the final catalysts was evaluated by digesting a 15 mg sample with HCl:HNO_3 (3:1) mixture inside an autoclave. These autoclaves were heated up to 200 ºC for 15 min using microwave irradiation. This digestion procedure was repeated three times to prepare the samples. After dilution, the metal loading was quantified using a microwave plasma-atomic emission spectrometer (4100 MP-AES, Agilent). X-ray photoelectron spectroscopy (XPS) was performed using a Kratos AXIS Ultra DLD spectrometer (Kratos Analytical Ltd., Durham, UK), where binding energies were calibrated using C 1 s (284.6 eV) as internal reference. Spherical aberration-corrected scanning transmission electron microscopy (C_S-corrected STEM) images were acquired using a high-angle annular dark-field (HAADF) detector in an FEI XFEG TITAN electron microscope at 300 kV equipped with a CETCOR C_S-probe corrector (CeOS GmbH, Germany). Electron-microscopy elemental analysis was carried out with an EDX detector (Oxford Instruments, UK) in scanning mode to produce electron-density mapping of the nanomaterial's surfaces (AZtec software, Oxford Instruments, UK).

2.3. Full range LED-assisted photocatalytic CO_2 hydrogenation tests

Photocatalytic tests were carried out in a prismatic quartz reactor in a fixed-bed configuration with sizes of 10 x 2 x 10 mm (Fig. 1). A mass of about 50 mg of powdered catalyst was located in the quartz reactor and a continuous gas stream of CO_2 and H_2 with a 1:4 molar ratio at an absolute pressure of 1.7 bar was passed through the fixed bed at 15 ml/min (in STP) during the experiment. Two equivalent high-irradiance LED lamps with variable emission wavelengths were located at both sides of the catalytic bed. These LED were alternatively set at UV light at 365 nm, white light in a RGB configuration and infrared light at 940 nm, with a constant DC current at 0.9 A and 12 V during irradiation [31,35,36]. The temperature of the reactor was continuously measured with a wire thermocouple placed inside the catalytic fixed bed and between LED emitters. During reaction tests, the temperature of the catalytic beds

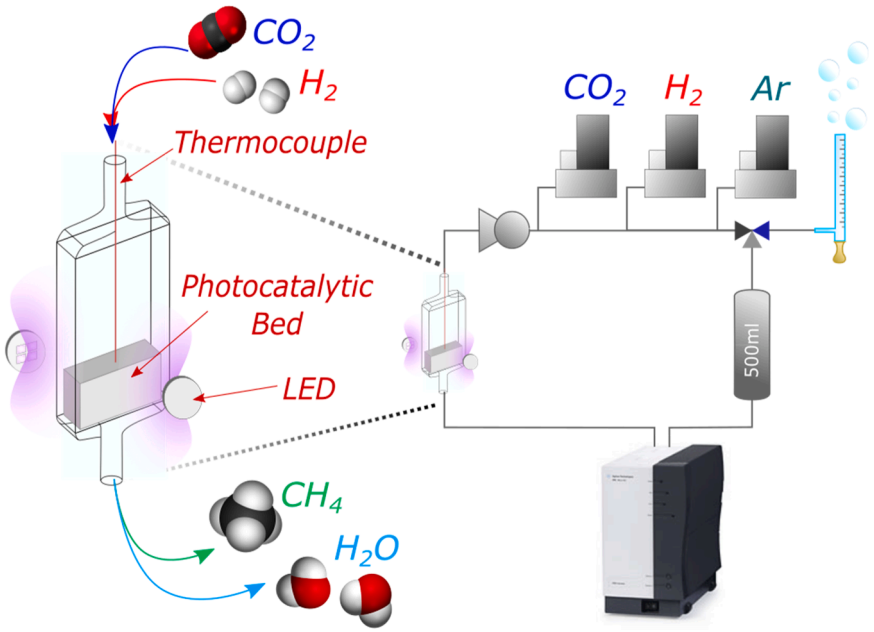

Fig. 1. Scheme of the fixed bed reactor configuration used for the photocatalytic CO_2 reduction tests under LED irradiation.

was controlled by adjusting the cooling airflow around the thermal diffusers of both LED emitters. Under this configuration, the photo-thermal effect for different irradiation wavelengths under the same temperature and pressure conditions was analyzed. Outlet gases were analyzed using an inline 490 micro-GC analyzer (Agilent Technologies, Santa Clara, CA) previously calibrated using a reference gas mixture bottle with known concentrations of the main possible reaction products and intermediates (Praxair). For the conventional thermal catalytic activation experiments, 50 mg of powdered solids were packed in a quartz tube adjusting the feed gas flow (1:4 CO_2:H_2 at 15 ml/min, $p = 1.7$ bar) and space time as in photocatalytic experiments. Similarly, bed temperature measured with a wire thermocouple immersed in the catalyst and fixed to 250 ºC with an electric furnace. The carbon mass balance was calculated from the sum of the carbon-containing gas species from the gas chromatograms to the amount of CO_2 gas feed to the reactor. In all cases, this mass balance was nearly 99 %.

2.4. *In situ analysis of the CO_2 hydrogenation process*

To better understand the CO_2 adsorption and hydrogenation processes over the studied catalysts, Diffuse Reflectance Infrared Fourier Transform Spectroscopy (DRIFTS) analysis was conducted using a Harrick Praying-Mantis catalytic chamber equipped with ZnSe windows coupled to a Bruker Vertex70 spectrometer. Before each analysis, the samples were submitted to thermal treatment at 150 ºC under vacuum for 1 h to remove ambient moisture. After drying, the samples were subjected to a thermal treatment under N_2 gas flow at 250 ºC to eliminate adsorbed CO_2, which was confirmed by the disappearance of the 2340 cm^{-1} bands of the ν_3 CO_2 vibration band. The DRIFTS analysis over catalysts was separated in two successive tests: first the CO_2 adsorption and subsequent CO_2 hydrogenation. For CO_2 adsorption tests at 250 ºC, dried materials were submitted at CO_2 gas flow at 15 ml/min and $p = 1$ bar and DRIFTS spectra were taken every 5 min up to 1 h of analysis. After this, CO_2 hydrogenation tests were conducted changing from the CO_2 gas flow to a CO_2/H_2 stream with a 1/4 ratio and $p = 1$ bar at 250 ºC, recording DRIFTS spectra every 5 min up to 1 h of analysis. All spectra were collected using a liquid nitrogen-cooled cadmium telluride detector, with 40 scans per measurement and a resolution of 4 cm^{-1}. The Kubelka-Munk algorithm was applied to the reflected intensity. All gas flows were controlled with Brooks 5844 mass flow controllers (Brooks Instruments, Hatfield, PA).

3. Results and discussion

3.1. *Characterization of the photodeposited materials*

Metallic Ni clusters were firstly photodeposited onto TiO_2 nanoparticles, obtaining an atomic loading of 1.6 at% for the Ni-TiO_2 catalyst. The Ru photo-assisted deposition led to an atomic loading of 0.5 at % (Fig. 2f). For the intermetallic Ru:Ni-TiO_2 catalyst, the Ni deposition was followed by a second photo-deposition of metallic Ru over the Ni-TiO_2 (Fig. 2a). This was performed since the difference in reduction potentials of Ni^{2+} ($E^0 = -0.257$ V) and Ru^{3+} ($E^0 = 0.2487$ V) cations led to inconsistent and non-replicable simultaneous co-deposition of both metals [37,38]. The partial replacement of Ni by Ru was identified by the increase in the light absorption in the near-infrared range in the absorption spectra of the solids after the sequential photo-deposition method (Fig. 2e). This sequential process enabled the galvanic replacement of a fraction of Ni atoms by Ru atoms, obtaining 0.43 at% Ni and 0.46 at% loadings (Fig. 2f). Although, the analysis of bulk metal concentration (Fig. 2f) showed that Ni was deposited in a larger extent than Ru, the surface concentration of this latter is higher than that of Ni (see XPS data of Table S1). This would suggest that Ni has a higher interaction with support upon photodeposition and could be buried to some extension in the TiO_2, as it has been reported [31].

The XRD patterns of the as-synthetized materials (see Figure S1 in supporting information) revealed that these retained the typical rutile and anatase diffraction peaks of P25 TiO_2 nanoparticles. This result indicated the small size and the good dispersion of the metallic particles deposited on the TiO_2 surface. The HAADF-STEM images of the catalysts showed that average diameters of metallic nanoparticles were 1.3 ± 0.4 nm for Ni-TiO_2, 0.96 ± 0.2 nm for Ru-TiO_2, whereas for Ru:Ni-TiO_2 were 1.23 ± 0.3 nm (see Figure S2). The EDX mapping revealed the good dispersion of both Ni and Ru motifs over the surface of TiO_2 support in relatively close positions (Figure S3), suggesting that photodeposition induced the formation of NiO clusters that could facilitate the secondary Ru^{3+} photoreduction due to the stabilization of charge carriers. Since electron microscopy images pointed out that Ru signals were rather concentrated around Ni atoms, the formation of bimetallic nanoparticles could be interpreted through a mechanism of galvanic

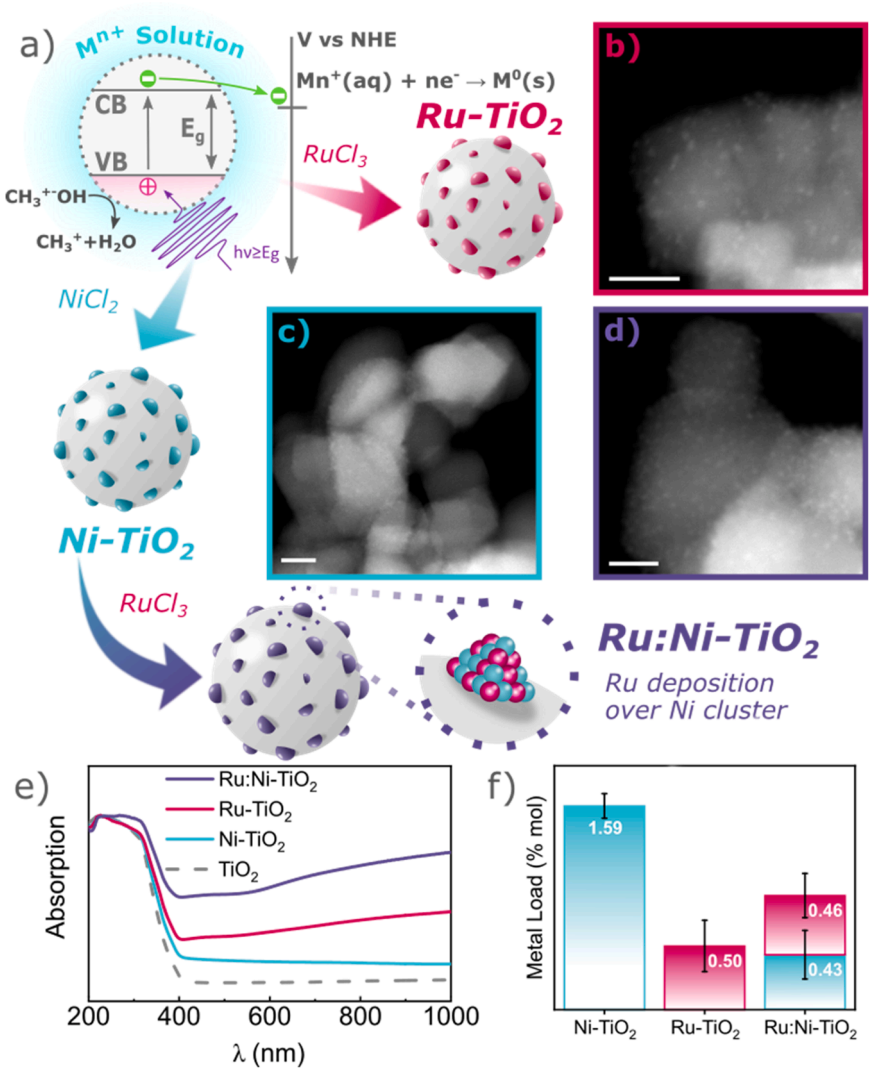

Fig. 2. (a) Scheme of the UV-LED driven photo-deposition method, with the metallic salts used as precursors and the two steps process used for the synthesis of Ru:Ni-TiO_2; HAADF-STEM images of the Ni-TiO_2 (b), Ru-TiO_2 (c) and Ru:Ni TiO_2 (d), where scale represent 10 nm; (e) UV-Vis absorption spectra of M-TiO_2 photocatalysts; (f) MP-AES metal load in mol%.

replacement of metallic Ni by Ru^{3+} cations [38]. Still, the resolution was not enough to distinguish whether bimetallic or intermetallic nanoparticles were formed.

3.2. Temperature programmed reduction tests

In order to have a deeper understanding of the Ni and Ru interaction

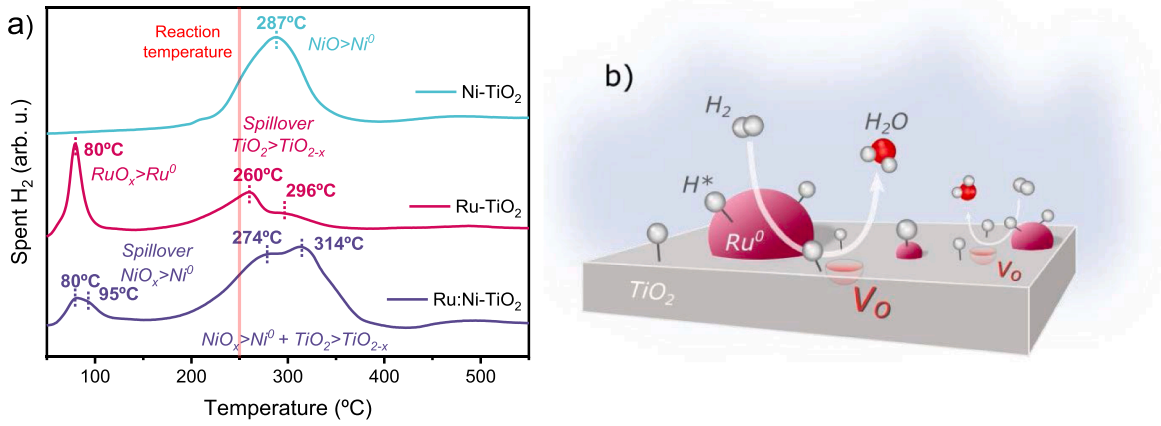

Fig. 3. (a) H_2-TPR study of the as-synthetized materials (20 ml/min, 10 % H_2:Ar, 10 °C/min up to 700 °C); (b) Scheme of the oxygen vacancy generation on the TiO_2 surface assisted by H_2 spillover driven by Ru sites.

with the TiO_2 support, a H_2-TPR study was carried out for the synthesized materials. The TPR curve of Ni-TiO_2 (Fig. 3a) shows a broad peak centered at 287 ºC, which can be assigned to the step reduction from Ni^{2+} to Ni^{+} and Ni^{0} of the photo-deposited nanoparticles [39,40]. For Ru-containing materials, two reduction peaks are observed: the first occurring below 100 ºC and the second between 220 ºC and 350 ºC. In the Ru-TiO_2, a sharp reduction signal arose at 80 ºC that corresponded to the reduction temperature of highly dispersed Ru oxide nanoparticles [41,42]. The second reduction signal can be attributed to the reduction of TiO_2 after the hydrogen spillover, favored by the deposited Ru nanoparticles [42–44]. Once reduced, the Ru nanosized clusters can induce the H_2 dissociation into radical H* species even at low temperatures [45,46]. These H* atoms could effectively displace the oxygen atoms in the TiO_2 surface to produce H_2O, thereby inducing the generation of oxygen vacancies (V_O) in TiO_2 (TiO_{2-x} in Fig. 3b) [3,45]. The reduction processes involving the Ru:Ni-TiO_2 can be attributed to the reduction of Ru oxides at temperatures below 100 ºC. Recent reports suggest the potential effect of Ru oxides to lower the reduction temperature of NiO due to hydrogen spillover [43,47–52]. Therefore, the shoulder observed would be consistent the reduction of Ni oxides nearby Ru centers [43,47–52]. Moreover, this suggests that Ni and Ru species are close on the TiO_2 support, as expected due to the galvanic replacement following the photo-deposition of Ni. In the second contribution, there is an overlap of the reduction of NiO without interaction with neighboring Ru atoms with the reduction of O^{2-} anions of the TiO_2 support due to the presence of Ru atoms [43,47].

3.3. XPS surface chemical analysis

The XPS surface chemical analysis showed that as-prepared materials were populated with Ti-O and Ti-OH moieties (Figs. 4d and 4e). The processes for deposition of metal units provoked no change in the TiO_2 sublattice, corroborating that those metal particles were effectively deposited onto the TiO_2 support [53–56]. Before reaction, the Ni nanoparticles deposited over the surface of Ni-TiO_2 were almost completely oxidized, except a 1.5 % of metallic Ni (see Table S1 for the fitting analysis of the O 1 s, Ti $2p_{3/2}$, Ni $2p_{3/2}$ and Ru $3d_{5/2}$ photoemission regions). For Ru-TiO_2 (Fig. 4a), the as-deposited Ru was completely oxidized (Fig. 4c). These features were attributed to the low content of methanol used in photodeposition that would lead to an oxidative process [42,57–60]. Under these conditions, the photogenerated positive charge carriers (holes or h^+) oxidized the sacrificial electron donor (methanol) in the ionic solution and the remaining photogenerated h^+ accelerated the photodeposition process, ruled by the following oxidative process:

$$M^{n+}(aq) + nh^{+} + nH_2O \rightarrow MO_n(s) + 2nH^{+}$$

where M^{n+} represent the metallic cations in the solution, and MO_n (s) are the metallic oxides deposited over the TiO_2 surface.

The TiO_2 support underwent few changes after the photocatalytic process. The relative positions of the Ti-O and Ti-OH signals were maintained, and no significant changes in the oxidation state of the support were observed. However, changes in the state of the photodeposited metal species (see Fig. 2 above) were observed after the photocatalytic reaction. The low fraction of metallic Ni disappeared after deposition of Ru in the Ru:Ni-TiO_2 catalyst before reaction. In contrast, a remarkable fraction of metallic Ru (34.1 %) was identified (Fig. 4c and Table S1), reinforcing the interpretation of the galvanic replacement process upon photodeposition [60–62]. After photocatalytic activity tests (*vide infra*), the metallic fraction of both Ni and Ru increased due to the reductive conditions of the reaction, except for Ni in the Ru:Ni-TiO_2. The atomic ratio of surface Ni/Ti and Ru/Ti in the mono metallic catalysts showed similar values before and after the photocatalytic experiments. For the bimetallic Ru:Ni-TiO_2, surface atomic ratios were cut by a 50 % and 24 % factor for Ni/Ti and Ru/Ti values

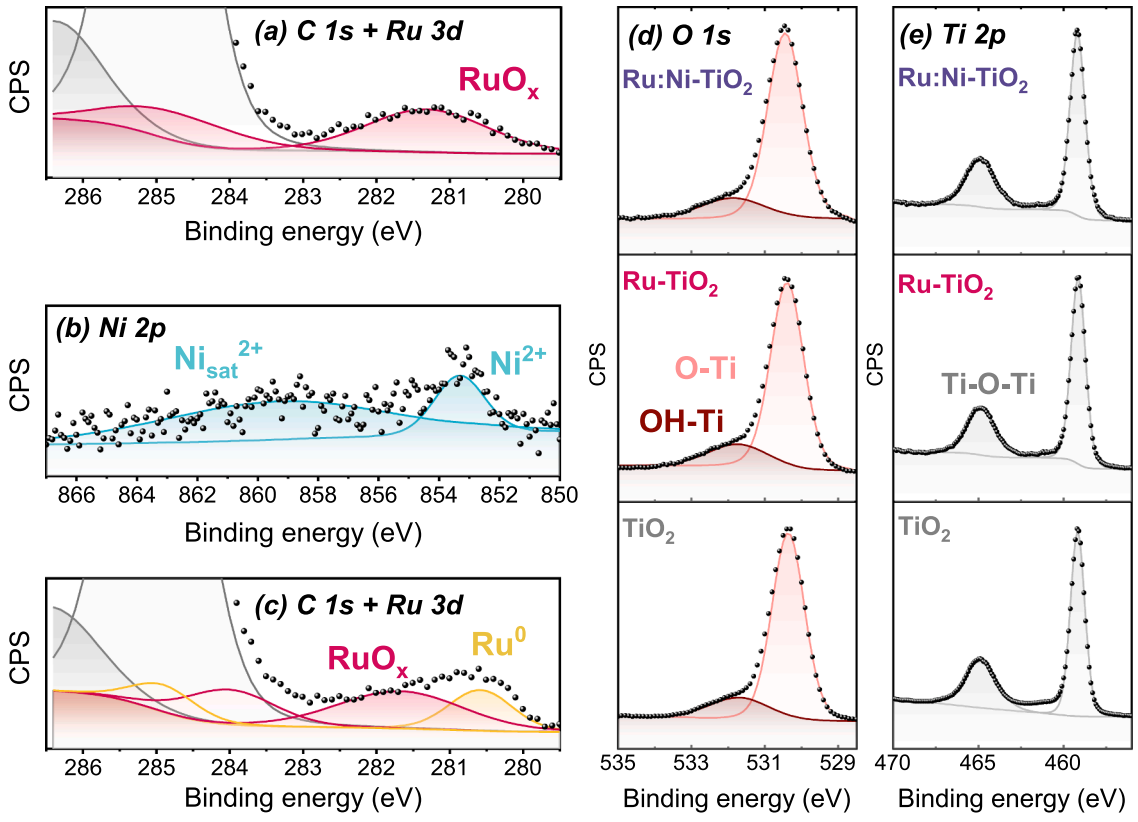

Fig. 4. XPS spectra of Ru:Ni-TiO_2 materials: (a) C 1 s + Ru 3d region of Ru-TiO_2, (b) Ni 2p region and (c) C1s + Ru 3d region of Ru:Ni-TiO_2, (d) O 1 s and (e) Ti 2p regions of Ru-TiO_2, Ru:Ni-TiO_2 and bare TiO_2 as a reference.

respectively. This reduction was ascribed to the partial sintering of the Ru:Ni nanoparticles under reaction conditions [63–65], which was confirmed by HAADF-STEM analysis where the size of these increased from 1.23 ± 0.4 nm to 1.94 ± 0.5 nm after photocatalytic activity tests (see Figure S2).

3.4. LED-driven photocatalytic CO_2 hydrogenation tests

The photocatalytic activity tests under different wavelength irradiation conditions over Ni:Ru-TiO_2 showed notable differences (Fig. 5). For instance, the reaction over Ni-TiO_2 induced similar productivities (about 1 mmol/g_{cat}h for both CO and CH_4) and selectivity profiles from ultraviolet to NIR. The CH_4 productivity progressively decayed with time, regardless of the irradiation wavelength used (Fig. 5a), while the CO productivity showed a nearly stable pattern. For Ru-TiO_2 (Fig. 5b), a remarkable increase in total productivity and selectivity to CH_4 was achieved in the early stages of the experiment, especially under NIR illumination (Fig. 5b) with total conversion under continuous flow conditions above 6 %. However, when illuminated under UV light during the first hour of the experiment, the selectivity to CH_4 dropped from 98 % to 55 % (Figure S5). Interestingly, when switching back to UV irradiation, the productivity profile also went back the trend marked in the first stage of UV irradiation, decreasing strongly for CH_4 and increasing for CO. A clear difference was then observed in productivity and selectivity to CH_4 in the visible and NIR irradiation steps, with selectivity values about 90 %. As UV–vis spectra showed (Fig. 2e), the absorption in visible and NIR regions is attributed to the deposition of Ru on TiO_2 and it can be expected that when irradiating with these wavelengths, the Ru particles (already reduced, as described in the TPR spectra in Fig. 3) were responsible for the light absorption. This change in the absorbed light wavelength, combined with the V_O generated at the TiO_2 surface due to the hydrogen spillover, would cause this change in selectivity. On the other hand, the Ru:Ni-TiO_2 photocatalyst maintained a CH_4 selectivity over 98 % throughout the whole the experiment, which could be attributed to the interaction between Ru and Ni [66,67].

3.5. Thermal catalytic CO_2 hydrogenation tests

To evaluate the contribution of light to the CO_2 hydrogenation process and discern it as photocatalytic or photo-thermal process, conventional non-irradiated continuous catalysis tests were additionally performed under the same reaction temperature and pressure conditions (Fig. 6). For monometallic Ni-TiO_2 and Ru-TiO_2, the reaction results were similar to the photocatalytic tests, showing that the initial selectivity towards CH_4 was progressively shifted to CO (Fig. 6 and Figure S6). Interestingly, CO_2 conversion rate over Ru-TiO_2 was 1.1 % under conventional catalysis conditions, much lower than the rate obtained under UV irradiation (3.3 % to the end of the experiment), under visible light irradiation (2.6 %) and under infrared irradiation (4.2 %). For this material, the increase in conversion rates and the differences observed by changing the irradiation wavelength at the same temperature highlights the photocatalytic contribution in the CO_2 hydrogenation. On the other hand, Ru:Ni-TiO_2 led to an almost complete selectivity towards CH_4 and the highest productivity among the studied materials, achieving about 9.5 mmol/g_{cat}h of CH_4 and a CO_2 conversion of 5.2 % at the end of the experiment. As described before, Ru^0 clusters would boost the H_2 dissociation even at low temperatures, thereby enhancing the hydrogenation of adsorbed CO_2 near the oxygen vacancies (V_O) and leading to improved selectivity to CH_4. On the other hand, the continuous formation of V_O on the surface of Ru-TiO_2 seemed to produce a high concentration of surface defects that, despite favoring CO_2 adsorption on the TiO_{2-x} surface, slowed down the hydrogenation process until it became negligible.

To clarify this apparent contradiction, CO_2 conversion and CH_4 selectivity data have been analyzed in different parts of the catalysis and photocatalysis experiments (Fig. 7). For Ni-TiO_2 and Ru-TiO_2,

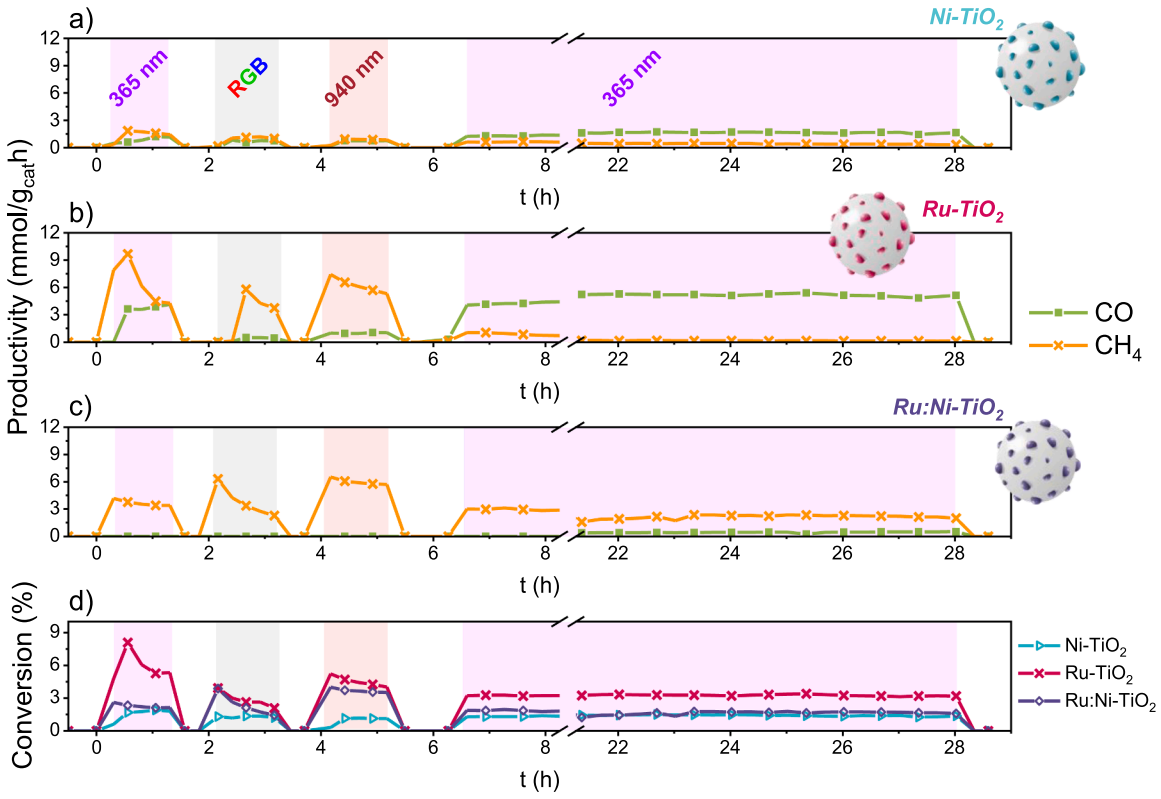

Fig. 5. Time evolution of the productivity (in mmol/g_{cat}·h) of CO and CH_4 of the continuous gas-phase photocatalytic CO_2 hydrogenation (CO_2/H_2 = 1/4, 15 ml/min in STP, p = 1.7 bar) over Ni-TiO_2 (a), Ru-TiO_2 (b) and Ru:Ni-TiO_2 (c); (d) Time evolution of the CO_2 conversion.

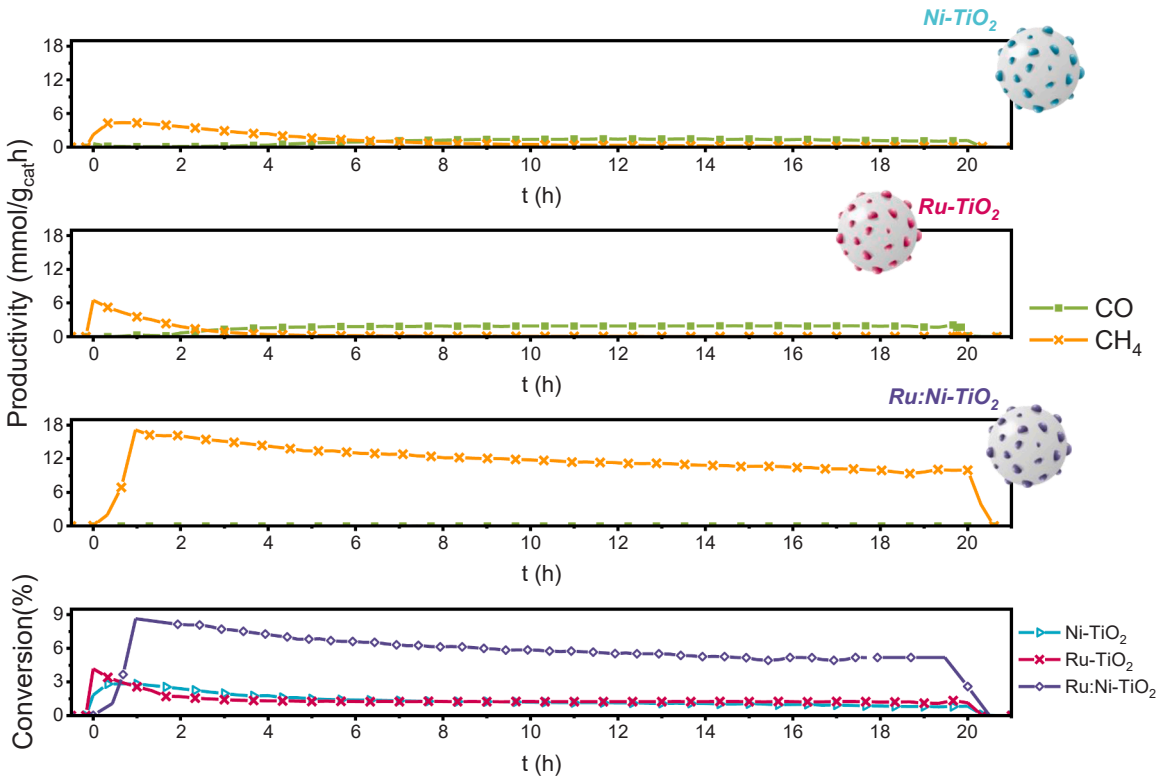

Fig. 6. Time evolution of the productivity (in mmol/g_{cat}·h) of CO and CH_4 of the continuous gas-phase CO_2 hydrogenation over Ni/TiO_2, Ru/TiO_2 and $Ru:Ni/TiO_2$ (CO_2/H_2 = 1/4, 15 ml/min in STP, p = 1.7 bar) and time evolution of the CO_2 conversion.

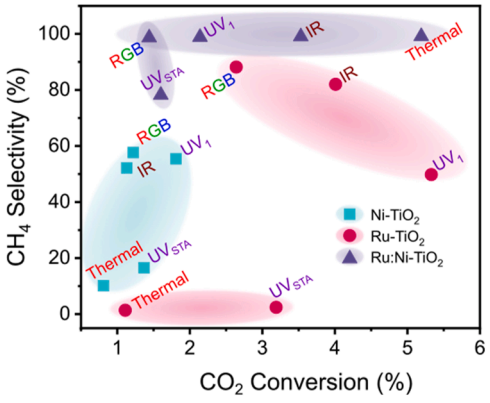

Fig. 7. Plot of CH_4 selectivity *vs.* CO_2 conversion obtained for the continuous CO_2 hydrogenation over $Ni-TiO_2$, $Ru-TiO_2$ and $Ni:Ru-TiO_2$ under either LED irradiation or thermal catalysis (CO_2/H_2 = 1/4, 15 ml/min in STP, p = 1.7 bar, T = 250 ºC). For photocatalytic tests, 'UV_1' represents the results from the first hour of irradiation under UV light, 'UV_{STA}' represents the results of the stable phase at the end of experiments under UV light, 'RGB' and 'IR' represents the results under RGB and IR LED. For the thermal tests, 'Thermal' represents the results in the last hour of the conventional thermal catalytic tests. As a visual help, shaded areas connect the results for every catalyst.

conversion values under photocatalytic conditions were always superior to those obtained under thermal catalysis conditions, suggesting that these materials were catalyzing the CO_2 reduction through a photocatalytic process. Actually, in terms of CH_4 selectivity, single-metal doped materials showed low CH_4 productivity under both LED irradiation and conventional thermal activation to the end of experiments.

The highest conversion and CH_4 selectivity results were obtained over $Ru:Ni-TiO_2$, with a nearly total yield of CH_4. Over this catalyst, the CO_2 conversion was higher under thermal catalysis than under photocatalytic conditions at any of the wavelengths tested. Nevertheless, the influence of the excitation wavelength seemed to be strong enough to enhance the values of CO_2 conversion even under IR light. This would suggest that the CO_2 hydrogenation on $Ru:Ni-TiO_2$ under the different LED lights follows a photo-thermal process.

In terms of the energy barrier of the thermal reaction, the activation energy over $Ru-TiO_2$ was about 25 kcal/mol while for $Ni-TiO_2$ and $Ni:Ru-TiO_2$ was slightly higher, around 45 kcal/mol (see Arrhenius plots in Figure S9 and Table S3). These values suggest are comparable to those found in literature for CO_2 reduction towards CO in a RWGS reaction [68,69].

Current gas-phase photocatalysts are based in TiO_2 as well as other metal oxide semiconductors decorated with different nanosized metal particles, which serve either as nano-heaters or as stabilizers of the electron-hole pairs. A quick look on the catalysis literature showed that the light activation of the photocatalyst was mostly done using solar simulator lamps with variable light irradiances and reaction temperatures (see Table 1 and references therein). In all reported cases, CO_2 hydrogenation mostly leads to CH_4 and CO as reaction products, with some reported cases of CH_3OH or C_2H_6 production. A closer look to the reported data points to the fact that most of catalysts and reactors give their maximum production at temperatures over 300ºC, at which CO_2 hydrogenation might also occur in the dark. Obviously, the energy consumption to produce a mole of reduced carbon fuels is also a factor consider in the design of efficient CO_2 reduction processes and there is a very wide dispersion on the irradiation intensities and reaction temperatures used.

3.6. *Identification of reaction intermediates by in situ DRIFTS analysis*

The CH_4 productivity observed over $Ru:Ni-TiO_2$ under UV and IR irradiation was comparable with those found in literature (see Table 1), even at higher irradiation and temperature conditions. More remarkable was the change in selectivity towards CH_4 over $Ru:Ni-TiO_2$, which

Table 1
Reported literature data of photothermal/photocatalytic CO_2 reduction over different metal-containing materials.

Catalyst	Reaction conditions	Light source	Irradiance, I (W/m^2)	CO_2 Conversion	Productivity (mmol/g·h)
Bi_2O_4/BiOBr nanosheets [70]	$NaHCO_3$ + H_2SO_4, 20 ºC	300-W Xe lamp	1530		2.5 (CO)
Co/Co-Al_2O_3nanosheets [71]	CH_4/CO_2 (1/1), 700 ºC	500-W Xe lamp (> 420 nm)	$3.54{\cdot}10^5$		25 (CO)
CoFeAl-LDH on Al_2O_3 [72]	CO_2/H_2/Ar (15/60/25), 300 ºC, 1.77 atm	300-W Xe lamp (200–800 nm)	216	**80 %** after 2 h	0.95 (CH_4)
M/Al_2O_3(M = Rh, Co, Pd) [73]	CO_2/H_2 (1/4), 350 ºC	300-W Xe lamp	428.6		20 (CH_4)
M-TiO_2 nanotubes (M = Au, Rh) [74]	CO_2/CH_4 (1/1), 130ºC	500-W Hg lamp (190–2000 nm)	2		1.7 (CO)
Ni/CeO_2 [75]	CO_2/CH_4 (1/1), 600ºC	500-W Xe lamp (200–2400 nm)	$3.63{\cdot}10^5$		6 (CO)
NiAl-LDH (H_2-reduced) [76]	CO_2/H_2/Ar (15/60/25), 290ºC, 1 atm	300-W Xe lamp (> 420 nm)	428.6	**80 %**	278.8 (CH_4)
Pd@Nb_2O_5 [13]	CO_2/H_2 (1/1), 470ºC	300-W Xe lamp	42		110 (CH_4)
Pt/CeO_2 mesoporous nanorods [77]	CO_2/CH_4 (1/1), 600ºC	500-W Xe lamp (200–2400 nm)	$3.71{\cdot}10^5$		6 (CO)
Ru/$NaTaO_3$ [78]	CO_2/H_2 (1/1), 0.8 atm	300-W Xe lamp (< 200 nm)	428.6		0.052 (CH_4)
Ru/Si Nanowires [79]	CO_2/H_2 (1/4), 150ºC	300-W Xe lamp	14500		0.8 (CH_4)
Ru@MgAl-LDH [16]	CO_2/H_2 (1/4), 350ºC	300-W Xe lamp	10000	**90 %**	277 (CH_4)
RuO_2/γ-Al_2O_3 (6 wt% Ru) [80]	CO_2/H_2 (1/5), 3.5 atm	Solar simulator	10100		60 (CH_4)
Ru-TiO_2 nanotubes [81]	CO_2/H_2 (1/4), 1.5 atm	Solar simulator	1000		2.4 (CH_4)
Ti-Silicalite [82]	CO_2/H_2 (1/3), 1 atm	Hg lamp (UV)	1000		0.003 (CH_4)
Ru:Ni-TiO_2 (this work)	CO_2/H_2 (1/4), 250ºC	LED (UV to IR)	1536 (UV) 980 (IR)	**3 %**	3.8 (CH_4 under UV) 5.77 (CH_4 under IR)

suggested different mechanisms for CO_2 hydrogenation. Indeed, in situ DRIFTS analysis performed over the catalysts under thermal reaction conditions confirmed several changes in the surface of catalysts (Fig. 8). The spectra from Ni-TiO_2 showed the band around 2077 cm^{-1}, associated to the physically adsorbed CO_2 molecules at 250 ºC (marked as CO_2* in Fig. 8), which increases in intensity as the exposure time to CO_2 increases 1 [83]. Similar trend was observed for the bands assigned to carbonyl groups located around 2020 and 1910 cm^{-1} (marked as Ni-CO in Fig. 8) [40,84–86]. Also, bridging carbonate groups are detected on the substrates (-CO_3 *b* at 1620–1670 cm^{-1}), together with monodentate carbonate (-CO_3 *m* at 1470–1530 cm^{-1}), bicarbonate (-CO_3H at 1400–1450 cm^{-1}) and formate (-CO_2H at 1330–1380 cm^{-1}) [40,84,85,87]. These bands could confirm the adsorption of CO_2 molecules through the hydroxyl terminal groups of the Ni-TiO_2 materials [88]. When exposed to the gas reaction mixture at 250 ºC, the band intensity of the adsorbed CO_2 and that of Ni-CO remained apparently unchanged (Fig. 8). However, there was a noticeable increase in the signals attributed to -CO_3 *m*, -CO_3H and -CO_2H, whereas the -CO_3 *b* remained at a more similar intensity. Since the reaction products observed under the CO_2 hydrogenation tests, both under illumination or heating, were CO and CH_4, the proposed reaction mechanism would involve the hydrogenation of adsorbed carbonate species over Ni clusters towards formate intermediates were further reduced to adsorbed CO (denoted CO*). Then the reaction can proceed to the complete hydrogenation of the CO* to CH_4, as seen at the initial steps over Ni-TiO_2 in thermal catalysis experiments. After a few hours, the hydrogenation of CO* intermediates was reduced and CO gas was the main reaction product.

Moreover, DRIFTS spectra of Ru-TiO_2 under reaction conditions revealed significant differences with respect to those of Ni-TiO_2. During the CO_2 adsorption step, spectra showed a stronger contribution of adsorbed -CO_3H species, together with weaker signals attributed to -CO_2H and -CO_3 *m* species. In contrast, -CO_3 *b* were absent (Fig. 8c), suggesting Ru co-catalyst would favor the slower hydrogenation of the adsorbed species than Ni. In addition to CO_2* at 2077 cm^{-1}, a band located around 2060 cm^{-1} was detected and assigned to carbonyl groups attached to Ru (Ru^{n+}-CO) [89,90]. Under reaction conditions, the relative intensity of CO_2* and Ru^{n+}-CO signals were stable and a band around 1880 cm^{-1}, associated to CO* was detected. The precise assignation of this latter band was challenging since the frequency is too low to be assigned to carbonyl groups adsorbed on Ru oxides, which are reported between 2200 and 2050 cm^{-1} [91]. In the literature, this band was assigned to linear carbonyl groups adsorbed on metallic Ru sites (Ru^0-CO) or as bridged Ru-CO on Ru clusters [92,93]. As mentioned above, the TPR analysis (Fig. 3) showed that Ru^{n+} to Ru^0 reduction occurred at 80ºC, pointing out that at 250 ºC the surface Ru was reduced. It is then reasonable to assign the 1880 cm^{-1} band to CO adsorbed onto Ru^0 in these conditions. The noticeable increase in the intensity of -CO_3 *m* and -CO_3H bands without the resulting increase in -CO_2H band would suggest the rise in the adsorption capacity that would be favored by the presence of oxygen vacancies (V_O). However, this feature would presume a lower hydrogenation capacity of the adsorbed intermediates under reaction conditions. Finally, the change in the evolution of reaction intermediates was in agreement with the increase in the selectivity to CO over Ru-TiO_2 under thermal catalysis.

For Ru:Ni-TiO_2, the direct adsorption of molecular CO_2 (CO_2*) and CO (CO*) could be also detected in the spectra (Fig. 8e). Again, bands attributed to -CO_3 *b* and -CO_3 *m*, together with -CO_3H and -CO_2H were clearly observed during the CO_2 adsorption step. Under the reaction mixture (Fig. 7f), the signal associated to adsorbed carbonates faded, leaving only the -CO_3H and -CO_2H bands. In addition, the CO_2* signal decreased and an intense CO* signal was detected suggesting that the combination of Ni and Ru would significantly accelerate the hydrogenation of adsorbed species to formate and then to carbonyl. This feature could explain the selectivity to CH_4 both in conventional thermal catalysis experiments and photocatalysis under LED irradiation. The absence of carbonate signals, expected reaction intermediates in CO_2 methanation [87], together with the decrease in CO_2* bands and the increase in those of CO* under a H_2-rich environment, would suggest a reaction mechanism where oxygen defects (V_O) in the TiO_2 support played a central role. This mechanism (Fig. 9) would consist of the adsorption of CO_2 occupying an oxygen vacancy, being released as CO gas or being hydrogenated until released as CH_4 [63]. This was consistent with the TPR results (Fig. 2), where the deposited Ru atoms on the TiO_2 surface induced the partial reduction of the TiO_2 support and the subsequent formation of oxygen vacancies (V_O) at the reaction temperature (250 ºC) utterly favored by the hydrogen spillover.

The CO_2 hydrogenation mechanism over the studied catalysts would therefore consist in the following adsorption and surface reaction sequence: -CO_3 → -CO_3H → -CO_2H → -CO → CH_4. The presence of reduced Ru in the surface would reduce the initial adsorption of carbonyl (-CO) species in comparison with Ni-loaded catalysts. However, preferential direct CO_2 adsorption was observed for Ru-containing materials in the form of bicarbonate (-CO_3H) species, along with the formation of carbonyl (-CO) on the surface under reaction conditions.

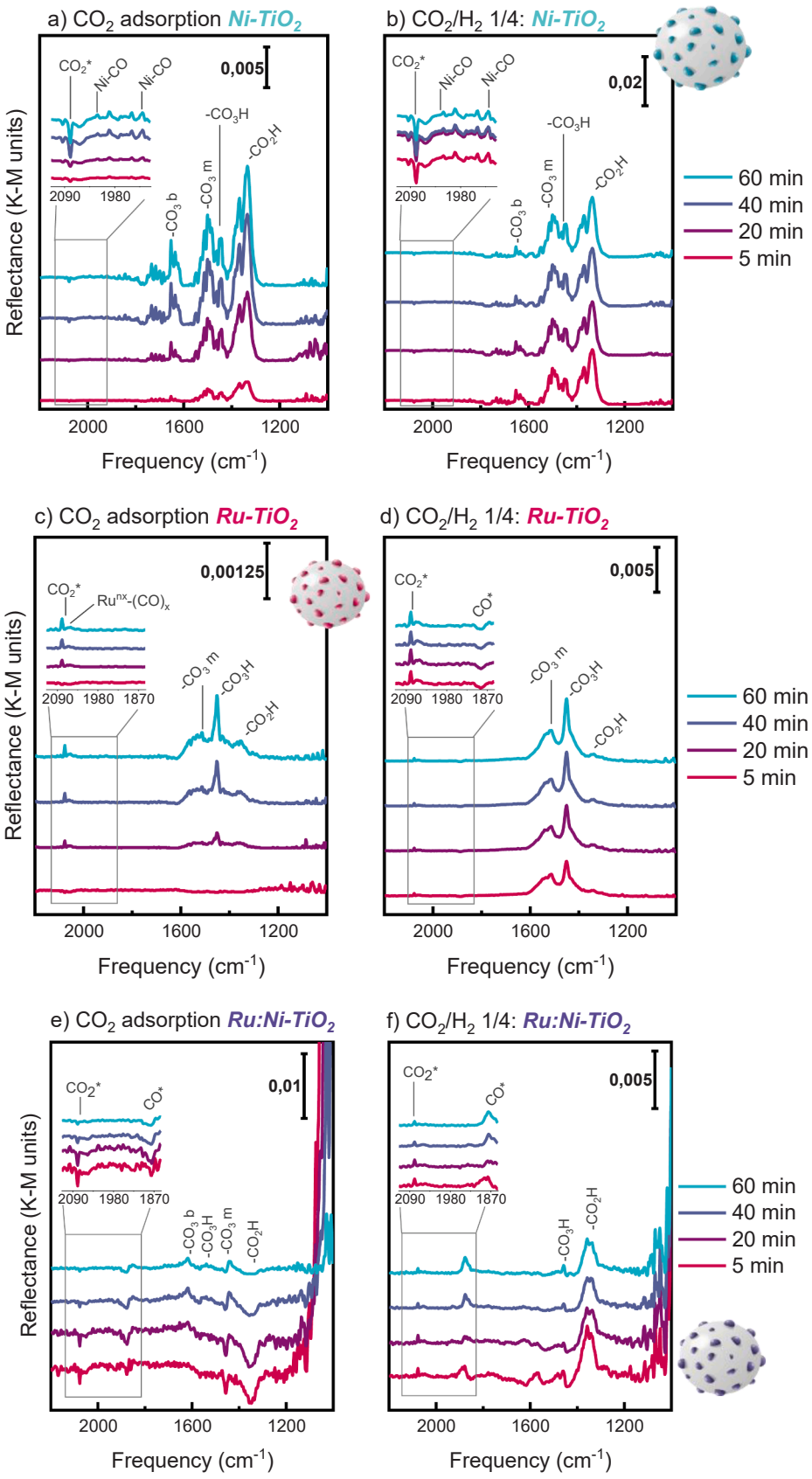

Fig. 8. In situ DRIFTS spectra of the thermal CO_2 gas adsorption (15 ml/min, $p = 1$ bar at 250 °C) and CO_2 hydrogenation (CO_2/H_2 1/4, $p = 1$ bar, 15 ml/min at 250 °C) over Ni-TiO_2 (a, b), Ru-TiO_2 (c, d) and Ru:Ni-TiO_2 (e, f).

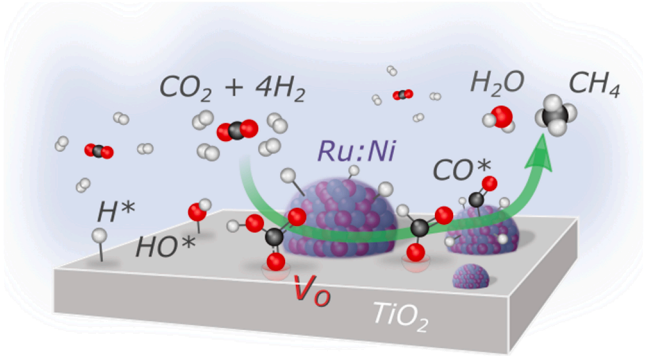

Fig. 9. Scheme of the proposed mechanism of CO_2 hydrogenation to CH_4 over the surface of Ru:Ni-TiO_2 assisted by the hydrogen spillover and subsequent generation of oxygen vacancies (V_O) on the TiO_2 surface.

Over these catalysts, the presence of oxygen vacancies (V_O) in the support, due to the hydrogen spillover on TiO_2, would accelerate the hydrogenation process. For Ru:Ni-TiO_2, the intermetallic clusters seemed to enhance the initial adsorption of CO_2 as both -CO and -CO_2H species, which further favored the methanation process. Similarly, the presence of these Vo in the vicinity of the intermetallic Ru-Ni clusters would increase the direct adsorption of CO_2 as CO*, which in turn would enhance the selectivity to CH_4.

4. Conclusions

The photo-assisted precipitation process under UV irradiation at 365 nm was effective for synthesizing highly dispersed Ni and Ru monometallic clusters over the surface of P25 TiO_2 nanoparticles. Ru introduction as a monometallic catalyst on TiO_2 enhanced photocatalytic performance towards CO_2 hydrogenation with respect to Ni with strong changes in selectivity depending on the irradiation wavelength. These features were due to the generation of oxygen vacancy defects (V_O) on TiO_2, after the hydrogen spillover facilitated by adsorbed Ru, which enhanced CO_2 adsorption and hydrogenation to CH_4 under visible and IR illumination. High selectivity to CO was otherwise preferred under UV light. Intermetallic Ru:Ni clusters deposited onto P25 TiO_2 nanoparticles notably improved the photocatalytic activity under NIR and maintain the selectivity to CH_4 under long irradiation periods at any of the wavelengths used, or even under thermal catalysis.

Single-metal catalysts (Ni-TiO_2 & Ru-TiO_2) favored CO_2 hydrogenation through a photocatalytic process, whereas over intermetallic Ru:Ni-TiO_2 the dominant process was the photothermal CO_2 hydrogenation. In all cases, these Ni:Ru-TiO_2 nanostructured catalysts provided outstanding results in terms of CO_2 conversion and selectivity towards CH_4, being of great interest for the development of photoactive systems for carbon capture and utilization technologies.

CRediT authorship contribution statement

Francisco Balas: Writing – review & editing, Writing – original draft, Supervision, Investigation, Data curation, Conceptualization. **Arturo Sanz-Marco:** Writing – review & editing, Writing – original draft, Software, Resources, Investigation, Funding acquisition, Formal analysis. **Jose L. Hueso:** Writing – review & editing, Validation, Supervision, Methodology, Investigation, Formal analysis, Conceptualization. **Jesus Santamaria:** Writing – review & editing, Validation, Supervision, Project administration, Investigation, Conceptualization. **Víctor Sebastian:** Writing – review & editing, Validation, Investigation.

Declaration of Competing Interest

The authors declare that they have no known competing financial interests or personal relationships that could have appeared to influence the work reported in this paper.

Acknowledgments

Financial support from the Spanish Ministry of Science and Universities through CEX2023–001286-S, PID2020–114926RB-I00, and CTQ2016–77144-R research projects are gratefully acknowledged. Researchers also thank collaboration through InterPHOT thematic network and “Conexion Fotocatalisis” CSIC hub. A. Sanz-Marco thanks the financial support for the MICINN Scholarship. We thank Dr. S. Irusta for her assistance in preliminary XPS measurements. The synthesis of materials has been performed by the Platform of Production of Biomaterials and Nanoparticles of the NANBIOSIS ICTS, more specifically by the Nanoparticle Synthesis Unit of the CIBER in Bioengineering, Biomaterials & Nanomedicine (CIBER-BBN). The TEM images were taken at the Laboratorio de Microscopias Avanzadas, Instituto de Nanociencia y Materiales de Aragon, Universidad de Zaragoza, Spain. The authors would like to acknowledge the use of Servicio General de Apoyo a la Investigación (SAI) of the Universidad de Zaragoza.

Appendix A. Supporting information

Supplementary data associated with this article can be found in the online version at doi:10.1016/j.cattod.2025.115440

Data Availability

Data will be made available on request.

References

[1] International Energy Agency, World Energy Oulook 2024, 2024. www.iea.org/terms (Accessed February 4, 2025).
[2] European Commission, The European Green Deal, Brussels, 2019. https://commission.europa.eu/strategy-and-policy/priorities-2019-2024/european-green-deal_en.
[3] L. Zhang, R. Li, L. Cui, Z. Sun, L. Guo, X. Zhang, Y.Y. Wang, Y.Y. Wang, Z. Yu, T. Lei, X. Jian, X. Gao, C. Fan, J. Liu, Boosting photocatalytic ammonia synthesis performance over OVs-Rich Ru/W18O49: insights into the roles of oxygen vacancies in enhanced hydrogen spillover effect, Chem. Eng. J. 461 (2023) 141892, https://doi.org/10.1016/j.cej.2023.141892.
[4] R.-P. Ye, J. Ding, W. Gong, M.D. Argyle, Q. Zhong, Y. Wang, C.K. Russell, Z. Xu, A. G. Russell, Q. Li, M. Fan, Y.-G. Yao, CO2 hydrogenation to high-value products via heterogeneous catalysis, Nat. Commun. 10 (2019) 5698, https://doi.org/10.1038/s41467-019-13638-9.
[5] J.-Y. Li, L. Yuan, S.-H. Li, Z.-R. Tang, Y.-J. Xu, One-dimensional copper-based heterostructures toward photo-driven reduction of CO2 to sustainable fuels and feedstocks, J. Mater. Chem. A 7 (2019) 8676–8689, https://doi.org/10.1039/C8TA12427B.
[6] M.N. Anwar, A. Fayyaz, N.F. Sohail, M.F. Khokhar, M. Baqar, A. Yasar, K. Rasool, A. Nazir, M.U.F. Raja, M. Rehan, M. Aghbashlo, M. Tabatabaei, A.S. Nizami, CO2 utilization: turning greenhouse gas into fuels and valuable products, J. Environ. Manag. 260 (2020) 110059, https://doi.org/10.1016/j.jenvman.2019.110059.
[7] J. Ashok, S. Pati, P. Hongmanorom, Z. Tianxi, C. Junmei, S. Kawi, A review of recent catalyst advances in CO2 methanation processes, Catal. Today 356 (2020) 471–489, https://doi.org/10.1016/j.cattod.2020.07.023.
[8] A. Álvarez, A. Bansode, A. Urakawa, A.V. Bavykina, T.A. Wezendonk, M. Makkee, J. Gascon, F. Kapteijn, Challenges in the greener production of formates/formic acid, methanol, and DME by heterogeneously catalyzed CO2 hydrogenation processes, Chem. Rev. 117 (2017) 9804–9838, https://doi.org/10.1021/acs.chemrev.6b00816.
[9] Y. Dong, R. Song, Z. Zhang, X. Han, B. Wang, S. Tao, J. Zhao, A.N. Alodhayb, Z. Chen, X. Yi, N. Zhang, Advances in photothermal CO2 hydrogenation catalysis for C1 molecules, Cell Rep. Phys. Sci. 5 (2024) 102227, https://doi.org/10.1016/j.xcrp.2024.102227.
[10] H. Zhang, Z. Xiao, P. Li, C. Zhang, X. Tan, F. Ye, J. Gu, E. Yuan, J.-J. Zou, D. Wang, LaCoO3 supported Pt for efficient photo-thermal catalytic reverse water-gas shift via the Mott-Schottky effect, Sep Purif. Technol. 350 (2024) 127998, https://doi.org/10.1016/j.seppur.2024.127998.
[11] Z. Xiao, L. Zhang, X. Tan, K. Sun, J. Li, L. Pan, J. Zou, G. Li, D. Wang, Advances in oxygen defect-mediated photothermal catalytic CO2 hydrogenation reduction, Adv. Funct. Mater. (2025), https://doi.org/10.1002/adfm.202500339.
[12] F. Sastre, A.V. Puga, L. Liu, A. Corma, H. García, Complete photocatalytic reduction of CO2 to methane by H2 under solar light irradiation, J. Am. Chem. Soc. 136 (2014) 6798–6801, https://doi.org/10.1021/ja500924t.

[13] J. Jia, H. Wang, Z. Lu, P.G. O'Brien, M. Ghoussoub, P. Duchesne, Z. Zheng, P. Li, Q. Qiao, L. Wang, A. Gu, F.M. Ali, Y. Dong, Q. Wang, K.K. Ghuman, T. Wood, C. Qian, Y. Shao, C. Qiu, M. Ye, Y. Zhu, Z. Lu, P. Zhang, A.S. Helmy, C.V. Singh, N. P. Kherani, D.D. Perovic, G.A. Ozin, Photothermal catalyst engineering: hydrogenation of gaseous CO2 with high activity and tailored selectivity, Adv. Sci. 4 (2017) 1700252, https://doi.org/10.1002/advs.201700252.
[14] L. Yuan, M. Qi, Z. Tang, Y. Xu, Coupling strategy for CO2 valorization integrated with organic synthesis by heterogeneous photocatalysis, Angew. Chem. Int Ed. 60 (2021) 21150–21172, https://doi.org/10.1002/anie.202101667.
[15] Z. Xiao, C. Zhang, J. Gu, E. Yuan, G. Li, J.-J. Zou, D. Wang, Designing Ni-In intermetallic alloy compounds for high activity and selectivity in low-temperature RWGS reaction, Chem. Eng. J. 507 (2025) 160529, https://doi.org/10.1016/j.cej.2025.160529.
[16] J. Ren, S. Ouyang, H. Xu, X. Meng, T. Wang, D. Wang, J. Ye, Targeting activation of CO2 and H2 over Ru-loaded ultrathin layered double hydroxides to achieve efficient photothermal CO2 methanation in flow-type system, Adv. Energy Mater. 7 (2017) 1601657, https://doi.org/10.1002/aenm.201601657.
[17] J. Zhou, H. Liu, H. Wang, Photothermal catalysis for CO2 conversion, Chin. Chem. Lett. 34 (2023) 107420, https://doi.org/10.1016/j.cclet.2022.04.018.
[18] R. Guo, C. Xia, Z. Bi, Z. Zhang, W. Pan, Recent progress of photothermal effect on photocatalytic reduction of CO2, Fuel Process Technol. 241 (2023) 107617, https://doi.org/10.1016/j.fuproc.2022.107617.
[19] S. Sarina, H.-Y. Zhu, Q. Xiao, E. Jaatinen, J. Jia, Y. Huang, Z. Zheng, H. Wu, Viable photocatalysts under solar-spectrum irradiation: nonplasmonic metal nanoparticles, Angew. Chem. Int. Ed. 53 (2014) 2935–2940, https://doi.org/10.1002/anie.201308145.
[20] F. Zhang, Y.-H. Li, M.-Y. Qi, Y.M.A. Yamada, M. Anpo, Z.-R. Tang, Y.-J. Xu, Photothermal catalytic CO2 reduction over nanomaterials, Chem. Catal. 1 (2021) 272–297, https://doi.org/10.1016/j.checat.2021.01.003.
[21] Y.-H. Li, J.-Y. Li, Y.-J. Xu, Bimetallic nanoparticles as cocatalysts for versatile photoredox catalysis, EnergyChem 3 (2021) 100047, https://doi.org/10.1016/j.enchem.2020.100047.
[22] E. Pena, J. Becerra, V.N. Gopalakrishnan, T.-O. Do, Facile one-pot synthesis of plasmonic gold nanoparticles decorated porphyrin-metal organic framework for photocatalytic hydrogen evolution, Mol. Catal. 548 (2023) 113470, https://doi.org/10.1016/j.mcat.2023.113470.
[23] W.A. Thompson, E. Sanchez Fernandez, M.M. Maroto-Valer, Probability Langmuir-Hinshelwood based CO2 photoreduction kinetic models, Chem. Eng. J. 384 (2020) 123356, https://doi.org/10.1016/j.cej.2019.123356.
[24] S. Al Jitan, G. Palmisano, C. Garlisi, Synthesis and surface modification of TiO2-based photocatalysts for the conversion of CO2, Catalysts 10 (2020) 227, https://doi.org/10.3390/catal10020227.
[25] D. Ješić, D. Lašič Jurković, A. Pohar, L. Suhadolnik, B. Likozar, Engineering photocatalytic and photoelectrocatalytic CO2 reduction reactions: mechanisms, intrinsic kinetics, mass transfer resistances, reactors and multi-scale modelling simulations, Chem. Eng. J. 407 (2021) 126799, https://doi.org/10.1016/j.cej.2020.126799.
[26] N. Shehzad, M. Tahir, K. Johari, T. Murugesan, M. Hussain, A critical review on TiO2 based photocatalytic CO2 reduction system: strategies to improve efficiency, J. CO2 Util. 26 (2018) 98–122, https://doi.org/10.1016/j.jcou.2018.04.026.
[27] S. Lettieri, M. Pavone, A. Fioravanti, L. Santamaria Amato, P. Maddalena, Charge carrier processes and optical properties in TiO2 and TiO2-based heterojunction photocatalysts: a review, Materials 14 (2021) 1645, https://doi.org/10.3390/ma14071645.
[28] K. Lorber, P. Djinović, Accelerating photo-thermal CO2 reduction to CO, CH4 or methanol over metal/oxide semiconductor catalysts, IScience 25 (2022) 104107, https://doi.org/10.1016/j.isci.2022.104107.
[29] H. Zhao, Q. Mao, L. Jian, Y. Dong, Y. Zhu, Photodeposition of earth-abundant cocatalysts in photocatalytic water splitting: methods, functions, and mechanisms, Chin. J. Catal. 43 (2022) 1774–1804, https://doi.org/10.1016/s1872-2067(22)64105-6.
[30] G. Chen, R. Li, L. Huang, Advances in photochemical deposition for controllable synthesis of heterogeneous catalysts, Nanoscale 15 (2023) 13909–13931, https://doi.org/10.1039/d3nr02475j.
[31] A. Sanz-Marco, J.L. Hueso, V. Sebastian, D. Nielsen, S. Mossin, J.P. Holgado, C. J. Bueno-Alejo, F. Balas, J. Santamaria, LED-driven controlled deposition of Ni onto TiO 2 for visible-light expanded conversion of carbon dioxide into C 1 –C 2 alkanes, Nanoscale Adv. 3 (2021) 3788–3798, https://doi.org/10.1039/D1NA00021G.
[32] K. Wenderich, G. Mul, Methods, mechanism, and applications of photodeposition in photocatalysis: a review, Chem. Rev. 116 (2016) 14587–14619, https://doi.org/10.1021/acs.chemrev.6b00327.
[33] W.M. Haynes, D.R. Lide, T.J. Bruno (Eds.), CRC Handbook of Chemistry and Physics, 95th ed., CRC Press, Boca Raton, FL, 2014.
[34] B.D. Anderson, J.B. Tracy, Nanoparticle conversion chemistry: Kirkendall effect, galvanic exchange, and anion exchange, Nanoscale 6 (2014) 12195–12216, https://doi.org/10.1039/C4NR02025A.
[35] C.J. Bueno-Alejo, J.L. Hueso, R. Mallada, I. Julian, J. Santamaria, High-radiance LED-driven fluidized bed photoreactor for the complete oxidation of n-hexane in air, Chem. Eng. J. 358 (2019) 1363–1370, https://doi.org/10.1016/j.cej.2018.09.223.
[36] H. Suarez, A. Ramirez, C.J. Bueno-Alejo, J.L. Hueso, Silver-copper oxide heteronanostructures for the plasmonic-enhanced photocatalytic oxidation of N-hexane in the visible-NIR range, Materials 12 (2019) 3858, https://doi.org/10.3390/ma12233858.
[37] K.D. Gilroy, A. Ruditskiy, H.-C.C. Peng, D. Qin, Y. Xia, Bimetallic nanocrystals: syntheses, properties, and applications, Chem. Rev. 116 (2016) 10414–10472, https://doi.org/10.1021/acs.chemrev.6b00211.
[38] G. Zhou, Y. Dong, D. He, Bimetallic Ru–M/TiO2 (M = Fe, Ni, Cu, Co) nanocomposite catalysts facribated by galvanic replacement: structural elucidation and catalytic behavior in benzene selective hydrogenation, Appl. Surf. Sci. 456 (2018) 1004–1013, https://doi.org/10.1016/j.apsusc.2018.06.206.
[39] O. Shtyka, R. Ciesielski, A. Kedziora, W. Maniukiewicz, S. Dubkov, D. Gromov, T. Maniecki, Photocatalytic reduction of CO2 Over Me (Pt, Pd, Ni, Cu)/TiO2 catalysts, Top. Catal. 63 (2020) 113–120, https://doi.org/10.1007/s11244-020-01241-y.
[40] D. Messou, V. Bernardin, F. Meunier, M.B. Ordoño, A. Urakawa, B.F. Machado, V. Collière, R. Philippe, P. Serp, C. Le Berre, Origin of the synergistic effect between TiO2 crystalline phases in the Ni/TiO2-catalyzed CO2 methanation reaction, J. Catal. 398 (2021) 14–28, https://doi.org/10.1016/j.jcat.2021.04.004.
[41] L.F. Bobadilla, A. Muñoz-Murillo, J. Gándara-Loe, A. Pérez, O.H. Laguna, L. M. Martínez T, A. Penkova, M.A. Centeno, J.A. Odriozola, Effect of noble metal addition over active Ru/TiO2 catalyst for CO selective methanation from H2 rich-streams, Int. J. Hydrog. Energy 48 (2023) 25065–25074, https://doi.org/10.1016/j.ijhydene.2022.07.072.
[42] J.H. Shin, G.J. Kim, S.C. Hong, Reaction properties of ruthenium over Ru/TiO2 for selective catalytic oxidation of ammonia to nitrogen, Appl. Surf. Sci. 506 (2020) 144906, https://doi.org/10.1016/j.apsusc.2019.144906.
[43] K. Shun, K. Mori, S. Masuda, N. Hashimoto, Y. Hinuma, H. Kobayashi, H. Yamashita, Revealing hydrogen spillover pathways in reducible metal oxides, Chem. Sci. 13 (2022) 8137–8147, https://doi.org/10.1039/d2sc00871h.
[44] W. Tolek, N. Nanthasanti, B. Pongthawornsakun, P. Praserthdam, J. Panpranot, Effects of TiO2 structure and Co addition as a second metal on Ru-based catalysts supported on TiO2 for selective hydrogenation of furfural to FA, Sci. Rep. 11 (2021) 9786, https://doi.org/10.1038/s41598-021-89082-x.
[45] Q. Wu, C. Shen, N. Rui, K. Sun, C.jun Liu, Experimental and theoretical studies of CO2 hydrogenation to methanol on Ru/In2O3, J. CO2 Util. 53 (2021) 101720, https://doi.org/10.1016/j.jcou.2021.101720.
[46] P. Schlexer, H.-Y.T. Chen, G. Pacchioni, CO2 activation and hydrogenation: a comparative DFT study of Ru10/TiO2 and Cu10/TiO2 model catalysts, Catal. Lett. 147 (2017) 1871–1881, https://doi.org/10.1007/s10562-017-2098-1.
[47] R. Rios-Escobedo, E. Ortiz-Santos, J.A. Colín-Luna, J.N. Díaz de León, P. del Angel, J. Escobar, J.A. de los Reyes, Anisole hydrodeoxygenation: a comparative study of Ni/TiO2-ZrO2 and commercial TiO2 supported Ni and NiRu catalysts, Top. Catal. 65 (2022) 1448–1461, https://doi.org/10.1007/s11244-022-01662-x.
[48] O.U. Valdés-Martínez, C.E. Santolalla-Vargas, V. Santes, J.A. de los Reyes, B. Pawelec, J.L.G. Fierro, Influence of calcination on metallic dispersion and support interactions for NiRu/TiO2 catalyst in the hydrodeoxygenation of phenol, Catal. Today 329 (2019) 149–155, https://doi.org/10.1016/j.cattod.2018.11.007.
[49] S. Masuda, K. Mori, T. Sano, K. Miyawaki, W. Chiang, H. Yamashita, Simple route for the synthesis of highly active bimetallic nanoparticle catalysts with immiscible Ru and Ni combination by utilizing a TiO2 support, ChemCatChem 10 (2018) 3526–3531, https://doi.org/10.1002/cctc.201800329.
[50] H. Yu, X. Yang, Y. Wu, Y. Guo, S. Li, W. Lin, X. Li, J. Zheng, Bimetallic Ru-Ni/TiO2 catalysts for hydrogenation of N-ethylcarbazole: role of TiO2 crystal structure, J. Energy Chem. 40 (2020) 188–195, https://doi.org/10.1016/j.jechem.2019.04.009.
[51] Z. Wang, C. Dong, X. Tang, X. Qin, X. Liu, M. Peng, Y. Xu, C. Song, J. Zhang, X. Liang, S. Dai, D. Ma, CO-tolerant RuNi/TiO2 catalyst for the storage and purification of crude hydrogen, Nat. Commun. 13 (2022) 4404, https://doi.org/10.1038/s41467-022-32100-x.
[52] O.U. Valdés-Martínez, V.A. Suárez-Toriello, J.A. de los Reyes, B. Pawelec, J.L. G. Fierro, Support effect and metals interactions for NiRu/Al2O3, TiO2 and ZrO2 catalysts in the hydrodeoxygenation of phenol, Catal. Today 296 (2017) 219–227, https://doi.org/10.1016/j.cattod.2017.04.007.
[53] M. Baruah, S.L. Ezung, S. Sharma, U. Bora Sinha, D. Sinha, Synthesis and characterization of Ni-doped TiO2 activated carbon nanocomposite for the photocatalytic degradation of anthracene, Inorg. Chem. Commun. 144 (2022) 109905, https://doi.org/10.1016/j.inoche.2022.109905.
[54] M. Shaban, A.M. Ahmed, N. Shehata, M.A. Betiha, A.M. Rabie, Ni-doped and Ni/Cr co-doped TiO2 nanotubes for enhancement of photocatalytic degradation of methylene blue, J. Colloid Interface Sci. 555 (2019) 31–41, https://doi.org/10.1016/j.jcis.2019.07.070.
[55] Y. Zhou, Q. Zhang, X. Shi, Q. Song, C. Zhou, D. Jiang, Photocatalytic reduction of CO2 into CH4 over Ru-doped TiO2: synergy of Ru and oxygen vacancies, J. Colloid Interface Sci. 608 (2022) 2809–2819, https://doi.org/10.1016/j.jcis.2021.11.011.
[56] M. Kuang, Y. Wang, W. Fang, H. Tan, M. Chen, J. Yao, C. Liu, J. Xu, K. Zhou, Q. Yan, Efficient nitrate synthesis via ambient nitrogen oxidation with Ru-doped TiO2/RuO2 electrocatalysts, Adv. Mater. 32 (2020) 2002189, https://doi.org/10.1002/adma.202002189.
[57] X. Yang, F. Tan, D. Wang, Q. Feng, D. Qiu, D. Dang, X. Wang, Entrapping Ru nanoparticles into TiO2 nanotube: insight into the confinement synergy on boosting pho-thermal CO2 methanation activity, Ceram. Int. 47 (2021) 27316–27323, https://doi.org/10.1016/j.ceramint.2021.06.153.
[58] N. Hamzah, N.M. Nordin, A.H.A. Nadzri, Y.A. Nik, M.B. Kassim, M.A. Yarmo, Enhanced activity of Ru/TiO 2 catalyst using bisupport, bentonite-TiO 2 for hydrogenolysis of glycerol in aqueous media, Appl. Catal. A Gen. 419420 (2012) 133–141, https://doi.org/10.1016/j.apcata.2012.01.020.
[59] A. Quindimil, U. De-La-Torre, B. Pereda-Ayo, A. Davó-Quiñonero, E. Bailón-García, D. Lozano-Castelló, J.A. González-Marcos, A. Bueno-López, J.R. González-Velasco, Effect of metal loading on the CO2 methanation: a comparison between alumina

supported Ni and Ru catalysts, Catal. Today 356 (2020) 419–432, https://doi.org/10.1016/j.cattod.2019.06.027.
[60] W. Tolek, N. Nanthasanti, B. Pongthawornsakun, Effects of - TiO 2 structure and Co addition as a second metal on Ru - based catalysts supported on - TiO 2 for selective hydrogenation of furfural to FA, Sci. Rep. (2021) 1–14, https://doi.org/10.1038/s41598-021-89082-x.
[61] X. Wang, P. Wu, Z. Wang, L. Zhou, Y. Liu, H. Cheng, M. Arai, C. Zhang, F. Zhao, Chlorine-Modified Ru/TiO2 catalyst for selective guaiacol hydrodeoxygenation, ACS Sustain Chem. Eng. 9 (2021) 3083–3094, https://doi.org/10.1021/acssuschemeng.0c07292.
[62] X. Gao, S. Zhu, M. Dong, J. Wang, W. Fan, Ru nanoparticles deposited on ultrathin TiO2 nanosheets as highly active catalyst for levulinic acid hydrogenation to γ-valerolactone, Appl. Catal. B Environ. 259 (2019) 118076, https://doi.org/10.1016/j.apcatb.2019.118076.
[63] J. Li, Y. Lin, X. Pan, D. Miao, D. Ding, Y. Cui, J. Dong, X. Bao, Enhanced CO2 methanation activity of Ni/anatase catalyst by tuning strong metal–support interactions, ACS Catal. 9 (2019) 6342–6348, https://doi.org/10.1021/acscatal.9b00401.
[64] O. Selcuk, B.S. Caglayan, A.K. Avci, Ni-catalyzed CO2 glycerol reforming to syngas: New insights on the evaluation of reaction and catalyst performance, J. CO2 Util. 67 (2023) 102329. https://linkinghub.elsevier.com/retrieve/pii/S2212982022004486 (accessed December 20, 2023).
[65] L. Lin, J. Liu, X. Liu, Z. Gao, N. Rui, S. Yao, F. Zhang, M. Wang, C. Liu, L. Han, F. Yang, S. Zhang, X.dong Wen, S.D. Senanayake, Y. Wu, X. Li, J.A. Rodriguez, D. Ma, Reversing sintering effect of Ni particles on γ-Mo2N via strong metal support interaction, Nat. Commun. 12 (2021) 6978, https://doi.org/10.1038/s41467-021-27116-8.
[66] Y. Pan, X. Han, X. Chang, H. Zhang, X. Zi, Z. Hao, J. Chen, Z. Lin, M. Li, X. Ma, Enhanced low-temperature CO 2 methanation over bimetallic Ni–Ru catalysts, Ind. Eng. Chem. Res 62 (2023) 4344–4355, https://doi.org/10.1021/acs.iecr.2c04560.
[67] M.A.A. Paviotti, B.M.M. Faroldi, L.M.M. Cornaglia, Ni-based catalyst over rice husk-derived silica for the CO2 methanation reaction: effect of Ru addition, J. Environ. Chem. Eng. 9 (2021) 105173, https://doi.org/10.1016/j.jece.2021.105173.
[68] S. Wang, J. Cai, I. Wang, Z. Li, An experimental and kinetic modeling study of CO2 hydrogenation to CO over Cu-Al catalyst utilizing MFB-TGA-MS, Carbon Capt. Sci. Technol. 10 (2024) 100163, https://doi.org/10.1016/j.ccst.2023.100163.
[69] Y. Cui, A. Labidi, X. Liang, X. Huang, J. Wang, X. Li, Q. Dong, X. Zhang, S. I. Othman, A.A. Allam, D.W. Bahnemann, C. Wang, Pivotal impact factors in photocatalytic reduction of CO2 to value-added C1 and C2 products, ChemSusChem 17 (2024) 202400551–202400552, https://doi.org/10.1002/cssc.202400551.
[70] D. Wu, L. Ye, S. Yue, B. Wang, W. Wang, H.Y. Yip, P.K. Wong, Alkali-induced in situ fabrication of Bi2O4-decorated BiOBr nanosheets with excellent photocatalytic performance, J. Phys. Chem. C. 120 (2016) 7715–7727, https://doi.org/10.1021/acs.jpcc.6b02365.
[71] S. Wu, Y. Li, Q. Zhang, Z. Jiang, Y. Yang, J. Wu, X. Zhao, High light-to-fuel efficiency and CO2 reduction rates achieved on a unique nanocomposite of Co/Co doped Al2O3 nanosheets with UV–vis-IR irradiation, Energy Environ. Sci. 12 (2019) 2581–2590, https://doi.org/10.1039/c9ee01484e.
[72] J. Zhao, R. Shi, G.I.N. Waterhouse, T. Zhang, Selective photothermal CO2 reduction to CO, CH4, alkanes, alkenes over bimetallic alloy catalysts derived from layered double hydroxide nanosheets, Nano Energy 102 (2022) 107650, https://doi.org/10.1016/J.NANOEN.2022.107650.
[73] X. Meng, T. Wang, L. Liu, S. Ouyang, P. Li, H. Hu, T. Kako, H. Iwai, A. Tanaka, J. Ye, Photothermal conversion of CO2 into CH4 with H2 over group VIII nanocatalysts: an alternative approach for solar fuel production, Angew. Chem. Int Ed. 53 (2014) 11478–11482, https://doi.org/10.1002/anie.201404953.
[74] B. László, K. Baán, E. Varga, A. Oszkó, A. Erdőhelyi, Z. Kónya, J. Kiss, Photo-induced reactions in the CO2-methane system on titanate nanotubes modified with Au and Rh nanoparticles, Appl. Catal. B Environ. 199 (2016) 473–484, https://doi.org/10.1016/j.apcatb.2016.06.057.
[75] Q. Zhang, M. Mao, Y. Li, Y. Yang, H. Huang, Z. Jiang, Q. Hu, S. Wu, X. Zhao, Novel photoactivation promoted light-driven CO2 reduction by CH4 on Ni/CeO2 nanocomposite with high light-to-fuel efficiency and enhanced stability, Appl. Catal. B Environ. 239 (2018) 555–564, https://doi.org/10.1016/j.apcatb.2018.08.052.
[76] Z. Li, R. Shi, J. Zhao, T. Zhang, Ni-based catalysts derived from layered-double-hydroxide nanosheets for efficient photothermal CO2 reduction under flow-type system, Nano Res. 14 (2021) 4828–4832, https://doi.org/10.1007/s12274-021-3436-6.
[77] M. Mao, Q. Zhang, Y. Yang, Y. Li, H. Huang, Z. Jiang, Q. Hu, X. Zhao, Solar-light-driven CO2 reduction by methane on Pt nanocrystals partially embedded in mesoporous CeO2 nanorods with high light-to-fuel efficiency, Green. Chem. 20 (2018) 2857–2869, https://doi.org/10.1039/c8gc01058g.
[78] M. Li, P. Li, K. Chang, T. Wang, L. Liu, Q. Kang, S. Ouyang, J. Ye, Highly efficient and stable photocatalytic reduction of CO2 to CH4 over Ru loaded NaTaO3, Chem. Commun. 51 (2015) 7645–7648, https://doi.org/10.1039/C5CC01124H.
[79] P.G. O'Brien, A. Sandhel, T.E. Wood, A.A. Jelle, L.B. Hoch, D.D. Perovic, C. A. Mims, G.A. Ozin, Photomethanation of gaseous CO2 over Ru/silicon nanowire catalysts with visible and near-infrared photons, Adv. Sci. 1 (2014) 1400001, https://doi.org/10.1002/advs.201400001.
[80] F. Sastre, C. Versluis, N. Meulendijks, J. Rodríguez-Fernández, J. Sweelssen, K. Elen, M.K. Van Bael, T. den Hartog, M.A. Verheijen, P. Buskens, Sunlight-fueled, low-temperature Ru-catalyzed conversion of CO2 and H2 to CH4 with a high photon-to-methane efficiency, ACS Omega 4 (2019) 7369–7377, https://doi.org/10.1021/acsomega.9b00581.
[81] M. Novoa-Cid, H.G. Baldovi, Study of the photothermal catalytic mechanism of CO2 reduction to CH4 by ruthenium nanoparticles supported on titanate nanotubes, Nanomaterials 10 (2020) 2212, https://doi.org/10.3390/nano10112212.
[82] S. Yamagata, M. Nishijo, N. Murao, S. Ohta, I. Mizoguchi, CO2 reduction to CH4 with H2 on photoirradiated TS-1, Zeolites 15 (1995) 490–493, https://doi.org/10.1016/0144-2449(95)00020-7.
[83] S.M. Fehr, I. Krossing, Spectroscopic signatures of pressurized carbon dioxide in diffuse reflectance infrared spectroscopy of heterogeneous catalysts, ChemCatChem 12 (2020) 2622–2629, https://doi.org/10.1002/cctc.201902038.
[84] M. González-Castaño, J. González-Arias, L.F.F. Bobadilla, E. Ruíz-López, J.A. A. Odriozola, H. Arellano-García, In-situ DRIFTS steady-state study of CO2 and CO methanation over Ni-promoted catalysts, Fuel 338 (2023) 127241, https://doi.org/10.1016/j.fuel.2022.127241.
[85] Z. Yan, Q. Liu, L. Liang, J. Ouyang, Surface hydroxyls mediated CO2 methanation at ambient pressure over attapulgite-loaded Ni-TiO2 composite catalysts with high activity and reuse ability, J. CO2 Util. 47 (2021) 101489, https://doi.org/10.1016/j.jcou.2021.101489.
[86] A. Álvarez, L.F. Bobadilla, V. Garcilaso, M.A. Centeno, J.A. Odriozola, CO2 reforming of methane over Ni-Ru supported catalysts: on the nature of active sites by operando DRIFTS study, J. CO2 Util. 24 (2018) 509–515, https://doi.org/10.1016/j.jcou.2018.01.027.
[87] A. Cárdenas-Arenas, A. Quindimil, A. Davó-Quiñonero, E. Bailón-García, D. Lozano-Castelló, U. De-La-Torre, B. Pereda-Ayo, J.A.A. González-Marcos, J.R. R. González-Velasco, A. Bueno-López, Isotopic and in situ DRIFTS study of the CO2 methanation mechanism using Ni/CeO2 and Ni/Al2O3 catalysts, Appl. Catal. B Environ. 265 (2020) 118538. https://linkinghub.elsevier.com/retrieve/pii/S0926337319312846 (accessed June 5, 2023).
[88] R. Zhou, N. Rui, Z. Fan, C.jun Liu, Effect of the structure of Ni/TiO2 catalyst on CO2 methanation, Int. J. Hydrog. Energy 41 (2016) 22017–22025, https://doi.org/10.1016/j.ijhydene.2016.08.093.
[89] P. Panagiotopoulou, Methanation of CO2 over alkali-promoted Ru/TiO2 catalysts: II. Effect of alkali additives on the reaction pathway, Appl. Catal. B Environ. 236 (2018) 162–170, https://doi.org/10.1016/j.apcatb.2018.05.028.
[90] J. Aßmann, E. Löffler, A. Birkner, M. Muhler, Ruthenium as oxidation catalyst: bridging the pressure and material gaps between ideal and real systems in heterogeneous catalysis by applying DRIFT spectroscopy and the TAP reactor, Catal. Today 85 (2003) 235–249, https://doi.org/10.1016/S0920-5861(03)00391-2.
[91] J. Zhang, M. Gao, R. Wang, X. Li, T. Huang, J. Wang, Y. Wang, Z. Zheng, Switching of CO2 hydrogenation selectivity via chlorine poisoning over Ru/TiO2 catalyst, Nano Res. 16 (2023) 4786–4792, https://doi.org/10.1007/s12274-022-5260-z.
[92] Z. Opre, J.D. Grunwaldt, M. MacIejewski, D. Ferri, T. Mallat, A. Baiker, Promoted Ru-hydroxyapatite: designed structure for the fast and highly selective oxidation of alcohols with oxygen, J. Catal. 230 (2005) 406–419, https://doi.org/10.1016/j.jcat.2004.12.012.
[93] E. Guglielminotti, F. Boccuzzi, An infrared study of Co adsorbed on a Ru/Zno catalyst, Stud. Surf. Sci. Catal. (1989) 437–446, https://doi.org/10.1016/S0167-2991(08)60706-5.